

The LISA beamline at ESRF

Francesco d'Acapito,^{a,*} Giovanni Orazio Lepore,^a Alessandro Puri,^a
Alessio Laloni,^{a,b} Fabrizio La Manna,^a Eric Dettona,^c Aleksander De Luisa^d and
Andrea Martin^d

^aCNR-IOM-OGG, c/o ESRF, LISA CRG, 71 Avenue des Martyrs, Grenoble, France, ^bESS, Odarslovsvagen 113, 224 84 Lund, Sweden, ^cESRF, 71 Avenue des Martyrs, Grenoble, France, and ^dCNR-IOM, Area Science Park, Strada Statale 14, km 163,5, I-34149 Trieste, Italy. *Correspondence e-mail: dacapito@esrf.fr

Received 12 October 2018

Accepted 28 December 2018

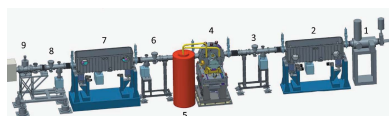
Edited by Y. Amemiya, University of Tokyo, Japan

Keywords: X-ray absorption spectroscopy; synchrotron radiation instrumentation; beamlines; LISA beamline.

This contribution provides a description of LISA, the new Italian Collaborating Research Group beamline operative at the European Synchrotron Radiation Facility. A presentation of the instruments available and optical devices is given as well as the main X-ray parameters (flux, energy resolution, focal spot dimensions, *etc.*) and comparison with theoretical calculations. The beamline has been open to users since April 2018 and will be ready at the opening of the Extremely Brilliant Source in late-2020.

1. Introduction

After the successful operation of the GILDA project (d'Acapito *et al.*, 1998, 2014) over the last two decades, the Italian Collaborating Research Group (CRG) beamline at the European Synchrotron Radiation Facility (ESRF) has been deeply renewed. Specifically, the X-ray optical scheme has been reviewed in order to open the possibility of new experimental techniques profiting from the considerable advancements occurring over the last few years, particularly in mirror technology. The new beamline has been named LISA [Linea Italiana per la Spettroscopia di Assorbimento X (Italian beamline for X-ray Absorption Spectroscopy)] and it is dedicated to X-ray absorption spectroscopy (XAS) and related techniques. The main goal was to realize a beamline with an intense (*i.e.* above 10^{10} photons s^{-1}) and small (sub-millimetre) beam in order to carry out XAS experiments in peculiar conditions such as highly dilute samples (Aucour *et al.*, 2015), high-quality low-noise transmission mode (Filipponi *et al.*, 2000), total reflection (Takakusagi *et al.*, 2013), pump-and-probe experiments (Chen *et al.*, 2003) and differential-mode (Amidani *et al.*, 2015). Other requirements were to have a wide energy range (~ 4 –70 keV) and an easy way to switch between high resolution and high luminosity. For all of this, a focalized beam exhibiting a particularly stable (spatially and temporally) position and energy scale was necessary. The central issue has been the choice of a focalization method ensuring beam homogeneity ('in focus' and 'off focus' positions), achromaticity and ease of setup; to that end the adoption of toroidal mirrors has been decided. This has been the case at several other beamlines, namely at APS (MacDowell *et al.*, 2004), B18 at DIAMOND (Dent *et al.*, 2009), the ROBL beamline at ESRF (Scheinost, 2017) and the CLAESS beamline at ALBA (Simonelli *et al.*, 2016). The alternative, consisting of a sagittally focusing monochromator [like in the GILDA (Pascarelli *et al.*, 1996) or FAME (Hazemann *et al.*, 2009) projects], was considered non-compliant



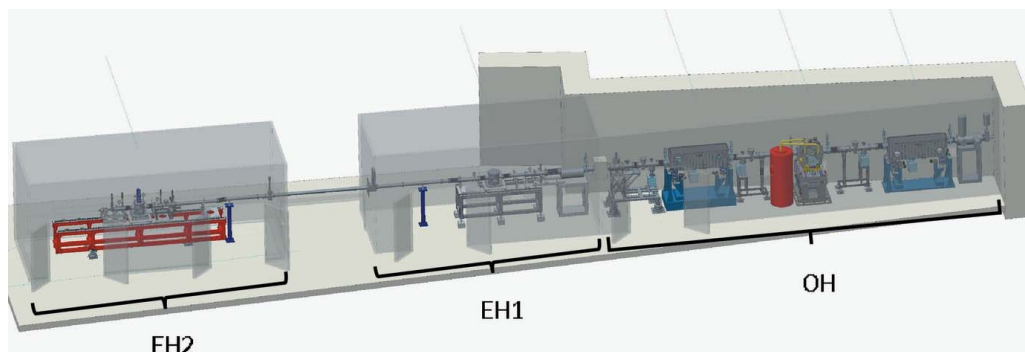


Figure 1
General layout of the LISA beamline. The center of the first hutch (optics hutch, OH) is about 28 m from the source, the first experimental hutch (EH1) is at 37 m and the second experimental hutch (EH2) is at 49 m.

with all the requirements of the new beamline. The main guidelines of the project were presented by d’Acapito & Trapananti (2017) and a mature project was presented by d’Acapito *et al.* (2016). Here, a description of LISA in the final version is given as well as the results of the commissioning runs with the main parameters and performance of the instrument.

2. Description of the beamline

LISA consists of three lead hutches: the optics hutch (OH) containing the main optical elements, the first experimental hutch (EH1) with the instrumentation for experiments with a non-focused beam and low-energy harmonic rejection mirrors, and finally the second experimental hutch (EH2) containing all the instrumentation for experiments with a focused beam (Fig. 1).

The center point of EH2 is at 49 m from the source and approximately coincides with the focal point of the focusing mirror, M2. All the experimental apparatus (slits, detectors, vacuum chambers) are supported by a 5 m-long bench and the vessels can be easily removed to make space for users’ instrumentation. EH1 is placed upstream with respect to EH2 at 37 m from the source. In this hutch a wide and homogeneous beam spot of $\sim 1 \text{ mm} \times 2 \text{ mm}$ can be obtained as it is sufficiently far from the focal point of M2. This can be useful

in the case of inhomogeneous samples and in cases when the maximum flux is not required.

2.1. The source

LISA takes the beam from a bending magnet of the ESRF ring with an electron beam energy of 6.03 GeV and a typical current of 200 mA (uniform filling mode). The magnet has a field of 0.85 T resulting in a critical energy of 20.6 keV. The source has dimensions of $78 \mu\text{m}$ (horizontally; H) by $36 \mu\text{m}$ (vertically; V) root mean square (r.m.s.) with emittance values of 8.5 nm (H) and 25 pm (V), and it is located at about 23 m from the principal slits; a $500 \mu\text{m}$ -thick Be window separates the beamline vacuum section from the machine. The thickness of this window is defined by the ESRF machine group and cannot be reduced in the present configuration of the front-end. In the typical angular range accepted by the beamline [1 mrad (H) and $50 \mu\text{rad}$ (V)] the total thermal load is about 50 W.

2.2. X-ray optics

The layout of the optics hutch with the position of the various elements is shown in Fig. 2. A vacuum vessel positioned upstream contains the principal slits and a set of attenuators ($100\text{--}500 \mu\text{m}$ C, $100\text{--}1000 \mu\text{m}$ Al, $100\text{--}250 \mu\text{m}$ Cu) that permits the thermal load on the subsequent optical

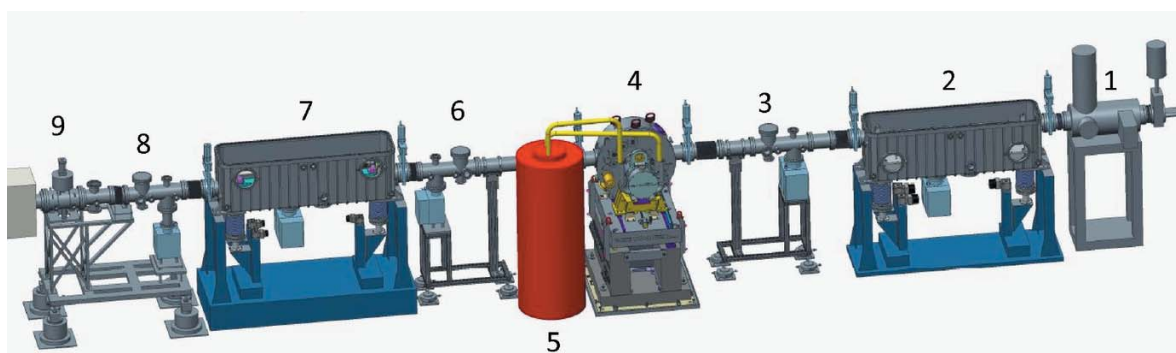


Figure 2
Side view of the optics hutch. The numbers label the different elements: 1, chamber with principal slits, attenuators and white beam monitor; 2, first mirror M1; 3, 6, 8, beam monitors; 4, monochromator; 5, cryocirculator; 7, second mirror M2; 9, beam shutter.

elements to be reduced. The first optical element is a collimating mirror M1, followed by the monochromator and by the focusing mirror M2. A pair of Pt-coated plane and parallel mirrors placed in EH1 achieve the harmonic suppression at energies below 11 keV. The mirrors were produced by THALES-SESO (Aix en Provence, France) whereas the monochromator was manufactured by CINEL (Vigonza, Italy).

M1 has a cylindrical shape and consists of a single-crystal Si substrate with two optical regions each 35 mm wide and 900 mm long; one exposing the silicon, the other coated with Pt. The mirror is located at ~ 24.9 m from the source and has a radius of curvature that can be varied, via a stepper motor, to maximize the beam collimation (theoretical meridional curvature radius $R_m^{M1} = 24.9$ km). Data from the manufacturer report a slope error below $0.5 \mu\text{rad}$ and a roughness below 2 \AA (r.m.s. values). The working angle for both M1 and M2 has been chosen to be 2 mrad because with this value the cutoff of the Si stripe (about 15 keV) is slightly above the L -absorption edges of Pt. In this way the reflectivity in the operating energy region for both surfaces contains no abrupt steps and it is possible to have a wide energy range with only two coatings. M1 is cooled with water via two copper blades inserted in longitudinal trenches filled with GaInSn liquid metallic alloy.

The monochromator is of the fixed-exit type with an offset of 15 mm and is equipped with two pairs of flat silicon crystals, one cut along the (311) planes and the other along the (111) planes. All the crystals are mounted on the same crystal cage so the change from one pair to the other can be carried out via a simple horizontal translation of the vacuum vessel. The angular operative range is $3.5\text{--}51^\circ$, thus allowing the energy range 2.5–32.5 keV to be reached with the Si(111) crystals, 4.9–72 keV with the Si(311) crystals and 7.6–97 keV with the Si(333) reflection [third harmonic of Si(111)]. An incremental encoder mounted on the last rotation stage (linked to the crystal cage) with resolution 22 nrad is used for the determination of the angular position. A single stepper motor drives at present the Bragg rotation but the design allows the installation of a direct current motor if operation in continuous scan mode is required. The second crystals have cascaded actuators for the pitch movement: a stepper motor for coarse positioning and a piezo for fine positioning. The piezo actuator of the pitch movement can be driven directly (manually changeable voltage) or inserted in a fast (analogic) feedback controller for the stabilization of the output intensity. In this latter case the working point (duty point) can be chosen either as a fixed absolute value of the readout of the I_0 ion chamber or a fixed position in the reflectivity curve by tracking in time the ring current. Two roll actuators (one per crystal) driven by stepper motors are also present on the second crystals. This permits the parallelism of the diffracting planes of each pair to be adjusted independently (planes are usually not perfectly aligned with the physical surfaces; in our case the misalignment was found to be less than 0.01°) permitting in this way horizontal drift of the beam to be avoided for different values of the Bragg angle.

The first crystals have dimensions of 40 mm (width; W) \times 48 mm (thickness; T) \times 140 mm (length; L) whereas the second crystals are 40 mm \times 37 mm \times 57 mm ($W \times T \times L$). The considerable thickness ensures a good resistance against mechanical deformation due to mounting. They are indirectly cooled by liquid nitrogen fed by an external cryocirculator [manufactured by CRIOTEC (Chivasso, Italy)] connected with the general liquid-nitrogen distribution network. The cooling circuit operates at a pressure stabilized at 2.8 bar (the peak-to-peak variation over several days is ~ 0.5 mbar) and the liquid flux is about 3.5 l min^{-1} .

The monochromator motion is controlled by *SPEC* (Certified Scientific Software, Cambridge, MA, USA; <https://certif.com>) using as the main variable the Bragg angle that defines the nominal energy (knowing the crystal type) and the crystal gap value to use. The Bragg angle is defined by the cumulated steps of the Bragg motor but this represents only a coarse determination of the angle (an offset is added to this value during the energy calibration procedures at the beginning of the experiments). The counts of the main Bragg encoder (stored in the raw datafile) are successively used by an offline routine to create the final and accurate energy scale; all XAS data shown hereafter have been treated in this way.

M2 is a double toroid and consists of a single substrate of crystalline silicon with two parallel cylindrical channels, one of which is coated with Pt. This mirror is located at 31.6 m from the source and its (fixed) sagittal radius is $R_s^{M2} = 45.8$ mm whereas the meridional radius R_m^{M2} can be varied with a stepper motor to match the theoretical value of 17.9 km. This permits the focalization of the beam at 17.9 m from the mirror inside the EH2 hutch. The focusing geometry is 2:1 and this value has been chosen in order to limit the total length of the beamline and to minimize the aberrations (MacDowell *et al.*, 2004). Both M1 and M2 have suitable external mechanics (stepper motor + encoder on the translations) for the definition of the incidence angle and the choice of the reflecting stripe. This is realized by three vertical actuators ('vertical' kinematical plane), whereas two more actuators realize the horizontal positioning plus yaw angle, all with a precision of $5 \mu\text{m}$. For accessing the highest part of the energy spectrum (>40 keV) the mirrors are removed and the monochromator lowered thanks to the vertically adjustable granite support (total stroke 15 mm).

In order to appropriately reject the harmonics in the lower part of the operating spectrum (mainly 4–6 keV) a pair of flat mirrors coated with Pt and working at 8 mrad are used, located in EH1. After this device, a second Be window of about $500 \mu\text{m}$ divides the high-vacuum section of the beamline (including the white beam path and the main optical elements) from the following low-vacuum sections. This window is considerably robust against accidental venting but it strongly limits the operating range of the beamline at low energy. In the case where a thinner Be window at the front-end is made available by the ESRF, the installation of a thinner window also at this point will be taken into consideration.

3. Experimental setup

The instruments for the data collection are grouped in two experimental hutches, EH1 and EH2. The former cabin (see Fig. 3) is close to the M2 mirror and it is used when a non-focused beam (dimensions of $\sim 1 \text{ mm} \times 2 \text{ mm}$) is desired. This cabin contains the vacuum vessel for the low-energies harmonic rejection mirrors and a vacuum chamber with a manipulator for the sample preceded and followed by ion chambers [length 150 mm (I_0) and 400 mm (I_1)]. These detectors are parallel plate chambers that can be filled with N_2 , Ar or Kr at a pressure varying from 0.1 to 1 bar. A manual distribution of gases is available for the users. The typical electric field value in the chambers is around 1 kV cm^{-1} . The signals from these chambers are read by picoamperometers and their output sent to the data acquisition computer via voltage-to-frequency converters. A support positioned laterally with respect to the vacuum chamber permits the installation of one of the high-purity germanium detectors available at LISA.

The subsequent experimental hutch EH2 is centered on the focal spot of M2 (see Fig. 4). Data in this position are collected with the fully focalized beam; no defocusing is envisaged here

as it was found to be quite difficult to obtain a homogeneous and regular shape for the unfocused beam here. If a large beam footprint on the sample is required then EH1 must be used. The instrumentation for data collection in EH2 consists of three ion chambers of length 100 mm similar to the ones previously described. Also here the gas type and pressure regulation is realized via a manually operated gas distribution line. For the collection of fluorescence from the samples, two high-purity germanium detector arrays (one with 12 elements, the other with 13 elements) are available for high energies ($E > 15 \text{ keV}$) whereas in the lower-energy range a four-channel silicon drift detector (SDD) is used (ARDESIA project; Bellotti *et al.*, 2018). In both cases the readout is made by digital analysis of the output pulses.

Experiments are carried out in vacuum chambers with manipulators hosting cold finger or cold chamber cryostats (temperature range from room temperature to 20 K) or a high-temperature reactor cell (MICROTOMO; Bellet *et al.*, 2003) up to 1300 K. The manipulators and sample environment devices can be easily exchanged between the two experimental hutches.

The control of the whole experimental setup is made via *SPEC* with graphical user interfaces for easier operation.

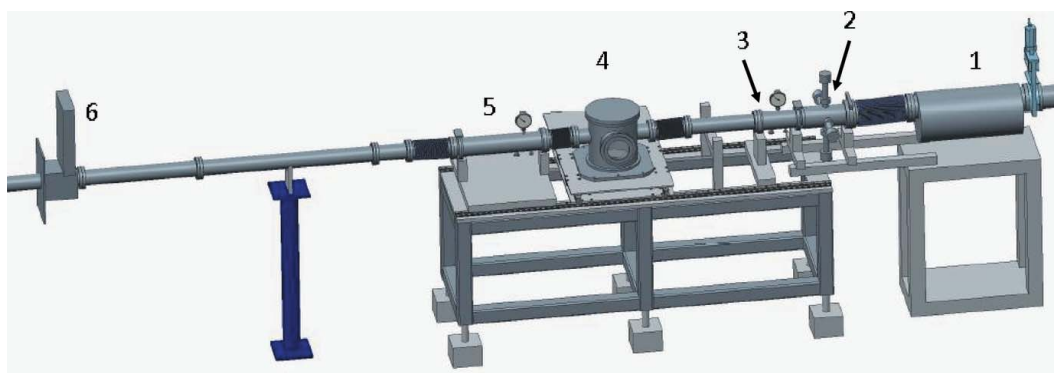


Figure 3 Side view of the EH1 cabin. Numbers label the various elements: 1, chamber with low-energy mirrors; 2, slits; 3, ion chamber I_0 ; 4, sample chamber; 5, ion chamber I_1 ; 6, shutter.

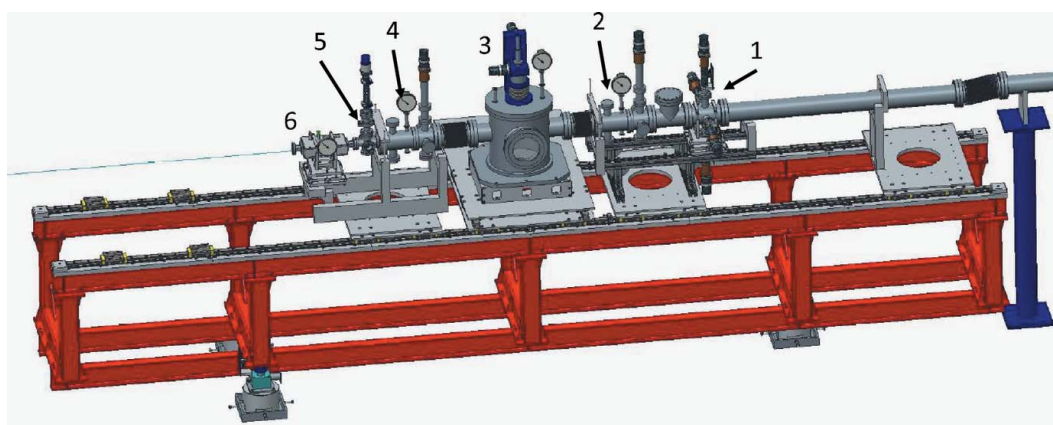


Figure 4 Side view of the EH2 cabin. Numbers label the various elements: 1, slits; 2, ion chamber I_0 ; 3, sample chamber; 4, ion chamber I_1 ; 5, reference foils holder; 6, ion chamber I_{ref} .

4. Performance

The performance of the beamline has been determined during a dedicated commissioning run and is summarized hereafter.

4.1. Energy resolution

A parameter of paramount importance for a spectroscopy beamline is the energy resolution. This depends on the crystal planes used for the data collection (Ishikawa *et al.*, 2005), but also on the thermal bump (Berman, 1995) and on the effective collimating power of the first mirror, especially when needing a high flux. The (meridional) radius of curvature of the first mirror R_m^{M1} has been optimized by collecting a series of spectra of a benchmark compound, in this case gaseous Br at the Br *K*-edge (13474 eV) (Filipponi *et al.*, 2000), with the Si(111) crystals. The pre-edge peak [originated by transitions to σ^* molecular orbitals (Heald & Stern, 1978)] has been successively fitted with a pseudo-Voigt function [using the approximation presented by Olivero & Longbothum (1977)] consisting of a Lorentzian with full width at half-maximum (FWHM) equal to 2.52 eV [the natural width as derived from Krause & Oliver (1979)] convoluted with a Gaussian of variable width. The results are shown in Fig. 5.

The minimum width of the Gaussian is obtained with a radius of curvature of ~ 30 km (according to the offsite manufacturer's calibration curve) in fair agreement with the expected value of 25 km. The resolution obtained ($\sim 1.7 \pm 0.1$ eV) is in good agreement with the intrinsic resolution of the Si(111) crystal, 1.75 eV at the Br *K*-edge energy [for Si(111) $\Delta E/E = 1.1 \times 10^{-4}$ (Ishikawa *et al.*, 2005)]. This means that even at the maximum vertical acceptance (high flux condition of the beamline) the energy resolution remains close to the theoretical predictions. The optimum radius was found to be the same if using the Pt or Si side of the mirror. With the optimized R_m^{M1} value the rocking curves of

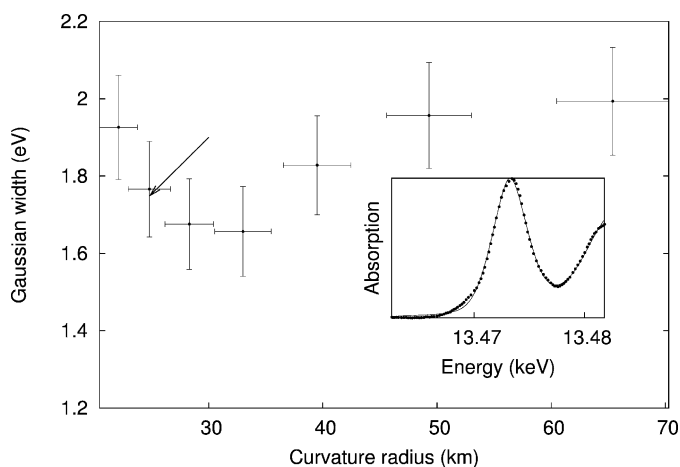


Figure 5

Width of the Gaussian component of the pseudo-Voigt line as a function of the meridional radius of curvature of M1, R_m^{M1} . Data were collected with the vertical principal slits at 2 mm so realizing a high-flux configuration (vertical divergence 90 μ rad). The point of the arrow marks the theoretical radius of curvature for perfect collimation and the theoretical value of the energy resolution (crystal intrinsic).

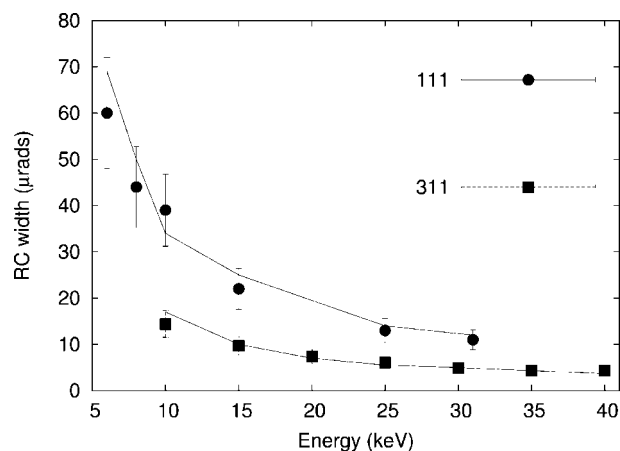


Figure 6

Rocking curve FWHMs. Points show experimental data, lines show theoretical calculations obtained by self-convoluting the rocking curves of single crystals calculated via the *XOP2.4* code (Sanchez del Rio & Dejus, 2011).

the two crystal sets at different energies were collected and their FWHM compared with the theoretical values, as shown in Fig. 6.

The measured data follow closely the theoretical calculations revealing that the principal sources of resolution degradation (namely, the crystal mechanical stress and/or the residual vertical divergence of the incoming beam) have a negligible contribution.

4.2. Flux

The flux available on the sample in focusing conditions has been measured in EH2 using N_2 - or Ar-filled ion chambers and is reported in Fig. 7. The values are in the 10^{11} photons s^{-1} range for the Si(111) crystal and in the 10^{10} photons s^{-1} range for the Si(311) crystal. The measured data follow satisfactorily

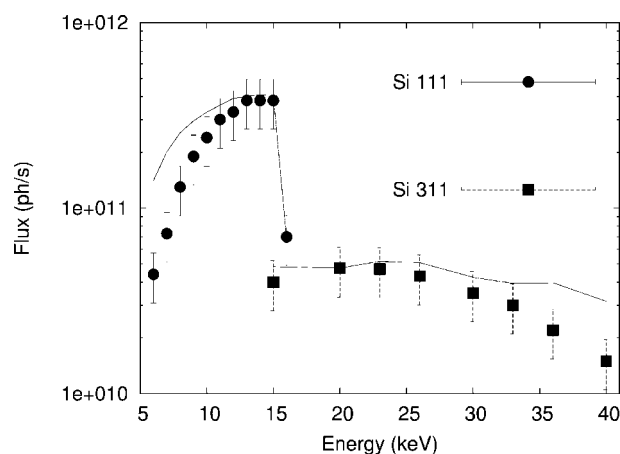


Figure 7

Flux available on the sample in focusing conditions using a Pt mirror for the Si(311) data and a Si mirror for the Si(111) data. Data measured with a storage ring current of 160 mA and principal slits open at 20 mm (H) and 1 mm (V). Points show experimental data (with error bars); lines show theoretical calculations.

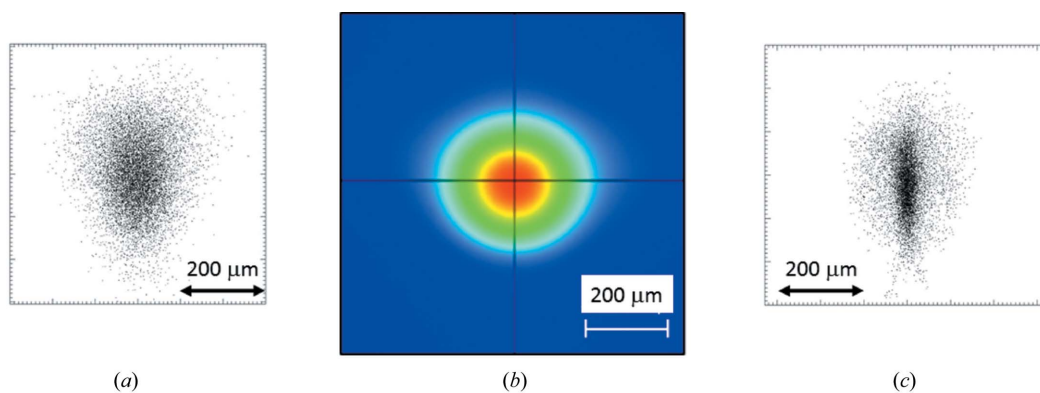


Figure 8 Theoretical and experimental beam spots. (a) Theoretical calculation for the present ESRF source (carried out with the source parameters presented in Section 2.1), (b) experimental spot, (c) calculated spot with the EBS source (data in Section 5). A ruler at 200 μm is also shown and is relative to both vertical and horizontal dimensions. Theoretical calculations were carried out with the *SHADOW3.0* code with a Si(111) crystal at 10 keV, with mirror surface errors taken from data on similar mirrors measured by the ESRF optics group.

the theoretical calculation, with deviations at the extremes of the accessible energy spectrum: at high energy (probably due to a higher mirror roughness than that stated by the manufacturer) and at low energies (due to higher-than-expected absorption from the Be windows).

4.3. Beam size

Simulations of the beam at the focal point with the final beamline parameter have been realized by X-ray tracing using the *SHADOW3* code (Sanchez del Rio *et al.*, 2011). The theoretical size is $\sim 120 \mu\text{m}$ (H) \times $180 \mu\text{m}$ (V) FWHM and is shown in Fig. 8.

The experimental data have been collected both with a high-resolution camera and with a blade scan, yielding in both cases a size of $\sim 170 \mu\text{m}$ (H) \times $180 \mu\text{m}$ (V) FWHM, in fair agreement with the theoretical predictions. This beam shape and the low divergence will allow the collection of data in the total reflection condition with the beam polarization parallel and perpendicular to the sample surface. As already stated, the use of the toroidal mirror also allows a large (millimetre-sized) and homogeneous beam to be obtained in the off-focus position (in our case the center of EH1) where XAS measurements can be carried out, namely on highly inhomogeneous samples. Fig. 9 shows a simulation of the beam in the EH1 sample chamber.

4.4. Energy stability and noise

In the collection of data in differential mode the stability of the energy scale is a parameter of pivotal importance. Energy shifts of the order of 10 meV at 10 keV can be sufficient to give rise to artifacts in the difference spectrum. The stability of the monochromator has been verified by subtracting two independent spectra of several compounds at different energy values and crystals; here we present the case of spectra collected on GeO_2 at the Ge *K*-edge collected with Si(111) crystals. The data were collected in the standard way using N_2 -filled ion chambers and feedback-stabilized output intensity. The result is shown in Fig. 10.

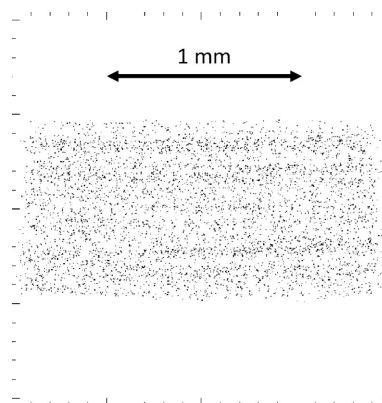


Figure 9 Theoretical beam spot in EH1, at about 6 m from M2. Theoretical calculations details are the same as for Fig. 8.

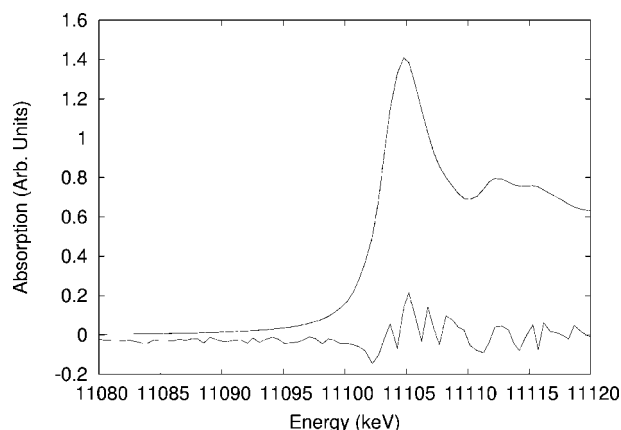
The difference between the two spectra shows no appreciable structures meaning that the energy calibration has remained stable in the short term of data collection (about 10 min per spectrum). In a period of several hours, however, shifts of the order of $1.5 \mu\text{rad}$ (tens of meV) have been observed as shown in Fig. 11.

The origin of this instability is currently under investigation. A final parameter determining the quality of the data is the residual noise obtainable in a transmission mode experiment. Fig. 12 shows an example spectrum for a titanium foil whereas an example spectrum for a silver foil is shown in Fig. 13.

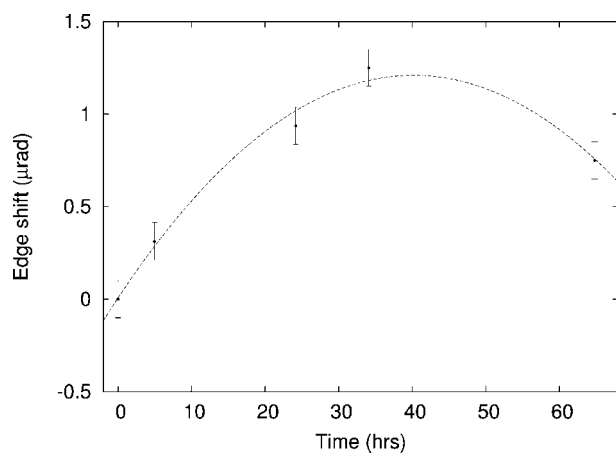
The residual noise on the Ti foil has been determined as 6×10^{-5} r.m.s., and the spectrum of Ag exhibits a slightly higher noise (1×10^{-4}) presumably due to the focused beam used. Overall the data quality is good and at the same level as previous reports (Filipponi *et al.*, 2000; Lützenkirchen-Hecht *et al.*, 2009).

5. Discussion and perspectives

The data presented here show that the design targets presented by d’Acapito & Trapananti (2017) have been met, namely in terms of beam size, intensity and energy range. The

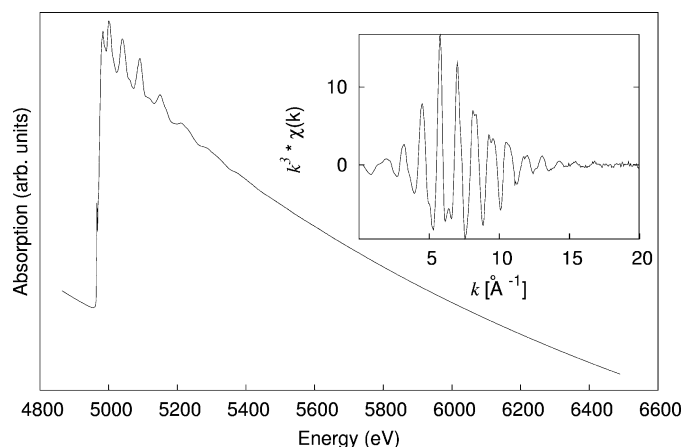

Figure 10

Two consecutive XANES spectra on a GeO_2 sample and related difference (multiplied by a factor of 100) collected at the Ge K -edge with Si(111) crystals. Data acquisition time was 3 s per point and the energy step on the edge was 0.5 eV. The choice of this compound comes from the coupling of two facts: a limited core-hole width (1.96 eV; Krause & Oliver, 1979) and a relatively small Bragg angle (10°) that result in a steep edge ideal for energy stability testing (the local derivative $D = \delta\mu/\delta\Theta_{\text{Bragg}}$ on a normalized $\Delta\mu = 1$ spectrum is about 300 degree^{-1}).

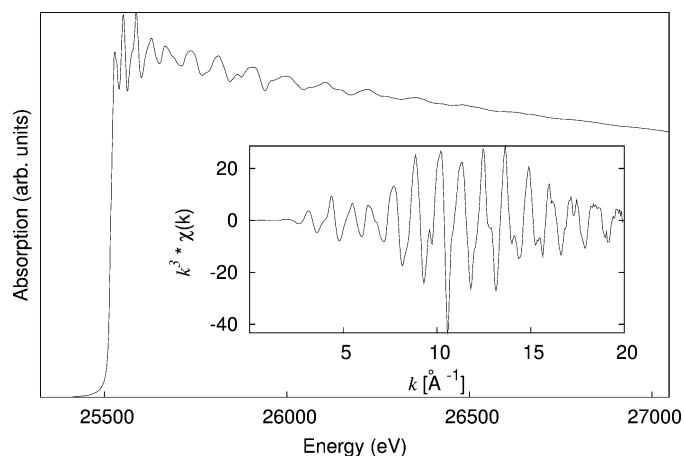

Figure 11

Evolution over time of the position of the Se K -edge in the case of a GeSe compound using a Si(111) crystal. The original data are EXAFS spectra extending over 800 eV above the edge and repeated over a few days. The precise position of the edge has been determined by shifting (angle from the Bragg encoder counts) one spectrum over the reference at $t = 0$ and minimizing the sum of squares of the point-to-point difference in the XANES region. Experimental data with the error bars are represented by points. The line is a guide for the eye.

energy resolution is close to the theoretical predictions even under the higher input divergence conditions, thus permitting the collection of highly resolved spectra even with high flux. The beam intensity follows the theoretical predictions except for the high and low ends of the spectrum where, for different reasons (presumably higher-than-expected roughness of the mirrors at high energy and absorption of Be windows at low energy), the measured values are somewhat lower than expected. The beam size is below $200 \mu\text{m}$ as required in the design. The angular (energy) shift with time (no shift observable in the short term, $1.5 \mu\text{rad}$ in the long term) and residual noise (between 10^{-4} and 10^{-5}) are considerably low.


Figure 12

Example of a spectrum of a Ti foil collected at room temperature with the Si(111) crystals in the off-focus position in EH1. The spectrum contains about 870 points and the total acquisition time was about 1 h. The inset shows the EXAFS signal up to 20 \AA^{-1} multiplied by a k^3 -weighting.


Figure 13

Example of a spectrum of an Ag foil collected at $T = 80 \text{ K}$ with the Si(311) crystals in the focus position in EH2. The spectrum contains about 570 points and the total acquisition time was about 35 min. The inset shows the EXAFS signal up to 20 \AA^{-1} multiplied by a k^3 -weighting.

The beamline will be perfectly compatible with the new EBS ring (Extremely Brilliant Source; Dimper *et al.*, 2014) as the sagittal radius of M2 has been chosen to place the focal point exactly in the middle of EH2 with the new source that will be placed 3 m upstream with respect to the present one. The source parameters will be $23 \mu\text{m}$ (H) and $3.6 \mu\text{m}$ (V) r.m.s. with emittance values of 0.5 nm (H) and 10 pm (V); the magnetic field will remain at 0.85 T. The input horizontal and vertical beam divergence values will also be compatible with those of EBS. The beamline will take the beam from a single bend source with the same critical energy as presently so the integrated flux will remain the same. The thermal load will not change appreciably due to the fact that the beam footprint on the optical elements and the integrated flux will remain the same. The horizontal beam size on the sample, on the other hand, is expected to decrease considerably (calculated size $35 \mu\text{m}$ FWHM) due to the reduction of the horizontal size of

the source; the vertical size will only be marginally affected (calculated size FWHM 170 μm) due to the shape error of the mirrors. After the shutdown of ESRF, LISA is expected to resume operation in the second half of 2020.

Acknowledgements

The authors thank the following people for help and advices during the design and realization phases of LISA: from ESRF, R. Baker, R. Barrett, Y. Dabin, M. Garrec, H. Gonzalez, R. Homs, R. Hino, A. Kaprolat, C. Morawe, M. Sanchez del Rio, T. N. Tran-Caliste, A. Vivo, R. Verbeni, H. Witsch; from CNR-IOM-Trieste, A. Morgante, F. Salvador, P. Bertoch; from Florence University, G. Fantappie, M. La Bella; from Fondazione Bruno Kessler, F. Rocca.

Funding information

LISA is financed by the Consiglio Nazionale delle Ricerche, project DFM.AD006.072.

References

- d'Acapito, F., Colonna, S., Pascarelli, S., Antonioli, G., Balerna, A., Bazzini, A., Boscherini, F. G. F. C., Chini, Dalba, G., Davoli, I., Fornasini, P., Graziola, R., Licheri, G., Meneghini, C., Rocca, F., Sangiorgio, L., Sciarra, V., Tullio, V. & Mobilio, S. (1998). *ESRF Newsl.* **30**, 42.
- d'Acapito, F. & Trapananti, A. (2017). *arXiv*:1702.00271.
- d'Acapito, F., Trapananti, A. & Puri, A. (2016). *J. Phys. Conf. Ser.* **712**, 012021.
- d'Acapito, F., Trapananti, A., Torrenco, S. & Mobilio, S. (2014). *Notiz. Neutroni Luce Sincrotrone*, **19**(2), 14.
- Amidani, L., Naldoni, A., Malvestuto, M., Marelli, M., Glatzel, P., Dal Santo, V. & Boscherini, F. (2015). *Angew. Chem. Int. Ed.* **54**, 5413–5416.
- Aucour, A.-M., Bedell, J.-P., Queyron, M., Magnin, V., Testemale, D. & Sarret, G. (2015). *Geochim. Cosmochim. Acta*, **160**, 55–69.
- Bellet, D., Gorges, B., Dallery, A., Bernard, P., Pereiro, E. & Baruchel, J. (2003). *J. Appl. Cryst.* **36**, 366–367.
- Bellotti, G., Butt, A. D., Carminati, M., Fiorini, C., Bombelli, L., Borghi, G., Piemonte, C., Zorzi, N. & Balerna, A. (2018). *IEEE Trans. Nucl. Sci.* **65**, 1355–1364.
- Berman, L. E. (1995). *Rev. Sci. Instrum.* **66**, 2041–2047.
- Chen, L. X., Shaw, G. B., Novozhilova, I., Liu, T., Jennings, G., Attenkofer, K., Meyer, G. J. & Coppens, P. (2003). *J. Am. Chem. Soc.* **125**, 7022–7034.
- Dent, A. J., Cibir, G., Ramos, S., Smith, A. D., Scott, S. M., Varandas, L., Pearson, M. R., Krumpa, N. A., Jones, C. P. & Robbins, P. E. (2009). *J. Phys. Conf. Ser.* **190**, 012039.
- Dimper, R., Reichert, H., Raimondi, P., Ortiz, L. S., Sette, F. & Susini, J. (2014). *ESRF Upgrade Programme Phase II (2015–2022) Technical Design Study*, http://www.esrf.fr/Apache_files/Upgrade/ESRF-orange-book.pdf.
- Filippini, A., Borowski, M., Bowron, D. T., Ansell, S., Di Cicco, A., De Panfilis, S. & Itiè, J. P. (2000). *Rev. Sci. Instrum.* **71**, 2422–2432.
- Hazemann, J.-L., Proux, O., Nassif, V., Palancher, H., Lahera, E., Da Silva, C., Braillard, A., Testemale, D., Diot, M.-A., Alliot, I., Del Net, W., Manceau, A., Gélébart, F., Morand, M., Dermigny, Q. & Shukla, A. (2009). *J. Synchrotron Rad.* **16**, 283–292.
- Heald, S. M. & Stern, E. A. (1978). *Phys. Rev. B*, **17**, 4069–4081.
- Ishikawa, T., Tamasaku, K. & Yabashi, M. (2005). *Nucl. Instrum. Methods Phys. Res. A*, **547**, 42–49.
- Krause, M. O. & Oliver, J. H. (1979). *J. Phys. Chem. Ref. Data*, **8**, 329–338.
- Lützenkirchen-Hecht, D., Wagner, R., Haake, U., Watenphul, A. & Frahm, R. (2009). *J. Synchrotron Rad.* **16**, 264–272.
- MacDowell, A. A., Celestre, R. S., Howells, M., McKinney, W., Krupnick, J., Cambie, D., Domning, E. E., Duarte, R. M., Kelez, N., Plate, D. W., Cork, C. W., Earnest, T. N., Dickert, J., Meigs, G., Ralston, C., Holton, J. M., Alber, T., Berger, J. M., Agard, D. A. & Padmore, H. A. (2004). *J. Synchrotron Rad.* **11**, 447–455.
- Olivero, J. & Longbothum, R. (1977). *J. Quant. Spectrosc. Radiat. Transfer*, **17**, 233–236.
- Pascarelli, S., Boscherini, F., D'Acapito, F., Hrdy, J., Meneghini, C. & Mobilio, S. (1996). *J. Synchrotron Rad.* **3**, 147–155.
- Sanchez del Rio, M., Canestrari, N., Jiang, F. & Cerrina, F. (2011). *J. Synchrotron Rad.* **18**, 708–716.
- Sanchez del Rio, M. & Dejus, R. J. (2011). *Proc. SPIE*, **8141**, 1–5.
- Scheinost, A. (2017). *The ROBL beamline at ESRF*, <http://www.hzdr.de/db/Cms?pNid=247>.
- Simonelli, L., Marini, C., Olszewski, W., Ávila Pérez, M., Ramanan, N., Guilera, G., Cuartero, V. & Klementiev, K. (2016). *Cogent Phys.* **3**, 1231987.
- Takakusagi, S., Chun, W.-J., Uehara, H., Asakura, K. & Iwasawa, Y. (2013). *Top. Catal.* **56**, 1477–1487.